nanomaterials

MDPI

Article

Flower-Like $MoSe_2/MoO_2$ Composite with High Capacity and Long-Term Stability for Lithium-Ion Battery

Qiuyan Hao [1], Guoliang Cui [1], Yan Zhao [1,*] and Zhumabay Bakenov [2]

[1] School of Materials Science and Engineering, Hebei University of Technology, Tianjin 300130, China
[2] Institute of Batteries LLC, National Laboratory Astana, Nazarbayev University, 53 Kabanbay Batyr Avenue, Nur-Sultan 010000, Kazakhstan
* Correspondence: yanzhao1984@hebut.edu.cn

Received: 24 July 2019; Accepted: 29 August 2019; Published: 5 September 2019

Abstract: A simple method is developed for the preparation of $MoSe_2/MoO_2$ composite with a flower-like structure for high-performance lithium-ion batteries (LIBs). $MoSe_2$ could lead to fast and facile movement of Li^+ due to its larger interlayer spacing. Meanwhile, MoO_2 could protect the lamellar structure of $MoSe_2$ from being destroyed in the charging/discharging processes to maintain the required active surface to electrolytes. In addition, the flower-like structure of the composite could effectively alleviate the volume expansion during charging/discharging. As LIBs are anode material, $MoSe_2/MoO_2$ composite demonstrates an excellent specific discharge capacity of 1042 mAh g^{-1} after 100 cycles at 0.1 A g^{-1}, which is attributed to the synergistic effects of $MoSe_2$ and MoO_2 in the composite.

Keywords: $MoSe_2/MoO_2$ composite; anode; LIBs; capacity; long-term cycle performance

1. Introduction

Lithium-ion batteries (LIBs) have been commercialized successfully in the past few decades and have made considerable progress in various fields, such as portable electronic products and energy storage devices for electric/hybrid vehicles [1–5]. Nonetheless, the commercial graphite anode is subjected to low specific capacity of 372 mAh g^{-1} and a slow insertion/extraction kinetics of Li^+, which seriously restricts the further application of LIBs in the development of electrical fields [6–8]. Up to now, the theoretical specific capacities of transition metal dihalogenated hydrocarbons and oxides are higher than carbon-based anodes, so they have been researched extensively as anode materials for LIBs [9–14]. Cao and coworkers reported a nanocomposite with Molybdenum dioxide (MoO_2) nanoparticles embedded into layered Molybdenum selenide ($MoSe_2$), delivering a reversible capacity of 520 mAh g^{-1} at 2 A g^{-1} after 400 cycles [15]. However, the preparation process of this anode is relatively complex.

$MoSe_2$ is a typical transition metal dichalcogenide, with a lamellar structure, which is similar to MoS_2 [16–18]. The layer spacing of $MoSe_2$ is 0.64 nm, which is larger than graphite (0.34 nm) and MoS_2 (0.62 nm) [19,20]. The large interlayer spacing of $MoSe_2$ favors the Li^+ intercalation/deintercalation process, but the large volume expansion leads to poor cyclic performance [21–25]. As a typical transition metal oxide, MoO_2 could also accomplish the Li^+ insertion/extraction process [26,27]. Meanwhile, MoO_2 possesses merits of low resistivity, high chemical stability, and electrochemical activity, so it has been used widely in the research of LIB anode materials [28–30].

Herein, we introduce a simple way of synthesizing a $MoSe_2/MoO_2$ composite as an advanced anode material. It is validated that the flower-like $MoSe_2/MoO_2$ composite exhibits excellent electrochemical

performance, attributing to the synergy of the homogeneous nanoscale composite. The combination of high specific capacity $MoSe_2$ and high electrochemically active MoO_2 make the composite exhibit great potential for LIBs.

2. Materials and Methods

2.1. Material Preparation

During the standard procedure, 2.0 mM Se powder and 0.8 mM Na_2MoO_4 were dissolved in 5 mL hydrazine hydrate and 15 mL deionized water, respectively, then two solutions were mixed and stirred evenly. The hydrothermal reaction was performed for the mixed solution at 160 °C for 24 h. After the reaction, the precipitate was washed alternately with ethanol and deionized water, and dried at 60 °C for 12 h. Then the temperature of the tube furnace was raised to 300 °C, the as-prepared $MoSe_2$ was calcinated for 5 min in a tube furnace in air atmosphere, and cooled to room temperature in the Ar atmosphere.

2.2. Characterization

The crystalline structure was tested using the X-ray diffractometer (XRD, Rigaku3014) with Cu-Kα1 radiation (λ = 0.15418 nm). The morphologies of the samples were observed by using a Nova NanoSEM 230 and a JEOL JEM-2100 TEM. The chemical composition of the samples was investigated by using X-ray photoelectron spectroscopy (XPS, Thermo ESCALAB 250) with an Al-Kα radiation. The Brunauer–Emmett–Teller (BET) surface area was tested by V-Sorb 2800P in an N_2 atmosphere.

2.3. Electrochemical Measurements

The electrochemical measurements were evaluated using CR-2032 coin cells. The active materials were mixed with conductive carbon and polyvinylidene fluoride (PVDF) at a weight ratio of 7:2:1 to prepare the electrodes. The resultant slurry wasspread on copper foil and dried in vacuum at 60 °C for 12 h, and the average mass loading of each electrode was about 2.4 mg cm^{-2}. CR2032 cells were assembled with lithium foil, electrolyte, and Celgard 2400 separator in an argon-filled glove box. The non-aqueous electrolyte consisted of 1 M lithium hexafluorophosphate ($LiPF_6$) dissolved in a mixed solution of ethylene carbonate/dimethyl carbonate (EC/DMC, 1:1 in volume). Galvanostatic charge-discharge measurements were performed on a CT2001A test system with a voltage range of 0.01–3 V. Cyclic voltammetry (CV) curves were tested on CHI605C electrochemical workstation (0.01–3 V; 0.1 mV s^{-1}). Electrochemical impedance spectroscopy (EIS) was executed at a frequency range of 0.01 Hz to 100 kHz on CHI660c electrochemical workstation.

3. Results and Discussion

The structural properties of the $MoSe_2/MoO_2$ composite are investigated by XRD in the 2θ range from 10 to 75°. Figure 1 shows the XRD patterns of the $MoSe_2/MoO_2$ composite, compared with the relevant PDF # 29-0914 and PDF # 32-0671, the hexagonal $MoSe_2$ phase with a space group of P63/mmc, and the monoclinic MoO_2 phase with a space group of P21/n are matched well with the PDF cards, respectively. The peaks at 2θ = 13.3°, 34.4°, 41.5°, 54.4° are ascribed to the (002), (100), (103), (110) planes of $MoSe_2$, respectively. The other three peaks at 26.0°, 37.1°, 53.5°, and 60,5°, are assigned to (11), (11), (22), and (013) planes of MoO_2, respectively. The crystallite sizes of the original $MoSe_2$ are calculated using the Scherrer formula to be 1.7 nm and increased to 3.8 nm after calcination. Consequently, the diffraction peaks of $MoSe_2$ in the $MoSe_2/MoO_2$ composite becomes sharp. These results suggest that the $MoSe_2/MoO_2$ composite has been successfully synthesized.

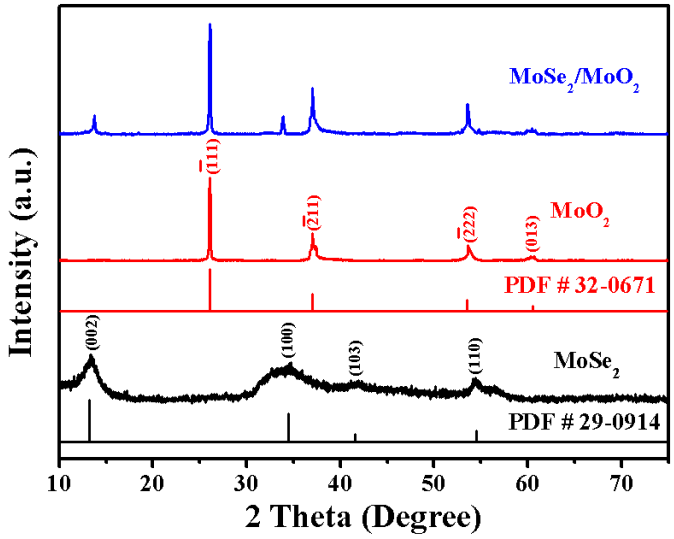

Figure 1. XRD pattern of $MoSe_2$, MoO_2, and the $MoSe_2/MoO_2$ composite.

Figure 2a shows the scanning electron microscopy (SEM) image of $MoSe_2$; it can be clearly observed that $MoSe_2$ exhibits a flower-like structure formed by the self-assembly of a lamellar structure. A crumpled feature of the $MoSe_2/MoO_2$ composite could be observed in Figure 2b, which is caused by the change of morphology after calcination in air atmosphere. Figure 2c shows the high resolution transmission electron microscope (HRTEM) image of the $MoSe_2/MoO_2$ composite. The lattice fringes with 0.65 and 0.24 nm spacing could be observed in the $MoSe_2/MoO_2$ composite, which corresponds to the (002) plane of $MoSe_2$ and (11) plane of MoO_2, respectively. Meanwhile, we could observe that there is a obvious interface between $MoSe_2$ and MoO_2 marked with pink dotted lines. EDX mapping of Mo, Se, and O elements are displayed in Figure 2d–f, indicating uniform distributions of Mo, Se, and O components over the $MoSe_2/MoO_2$ composite.

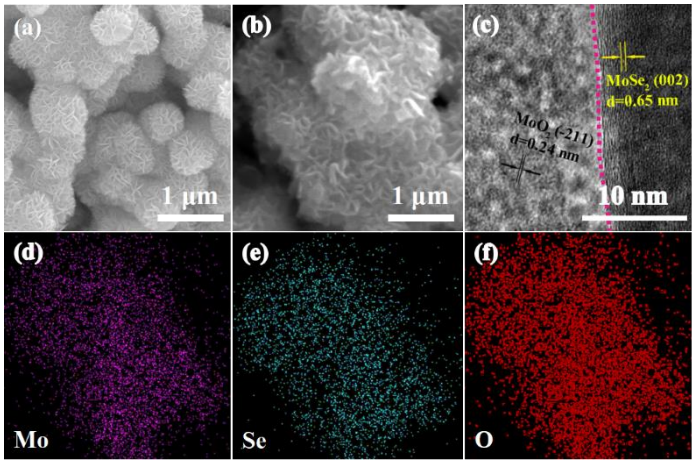

Figure 2. (**a**,**b**) SEM images of $MoSe_2$ and $MoSe_2/MoO_2$ composite; (**c**) HRTEM image of $MoSe_2/MoO_2$ composite; (**d**–**f**) EDX mapping of $MoSe_2/MoO_2$ composite.

The structural properties of $MoSe_2/MoO_2$ composite are determined by N_2 adsorption measurement. As shown in Figure 3a, the as-prepared $MoSe_2/MoO_2$ composite has a large surface area of 114 m^2 g^{-1}. The pore size distribution curve displays a narrow pore distribution of 2–4 nm, indicating there are abundant micropores and few mesoporous structures (Figure 3b). All the results show that the $MoSe_2/MoO_2$ composite has a high specific surface area and porosity; this is beneficial

for the infiltration of the electrolyte to electrode enhancing the charge transfer during the process of Li^+ insertion/extraction and adapting the huge volume change.

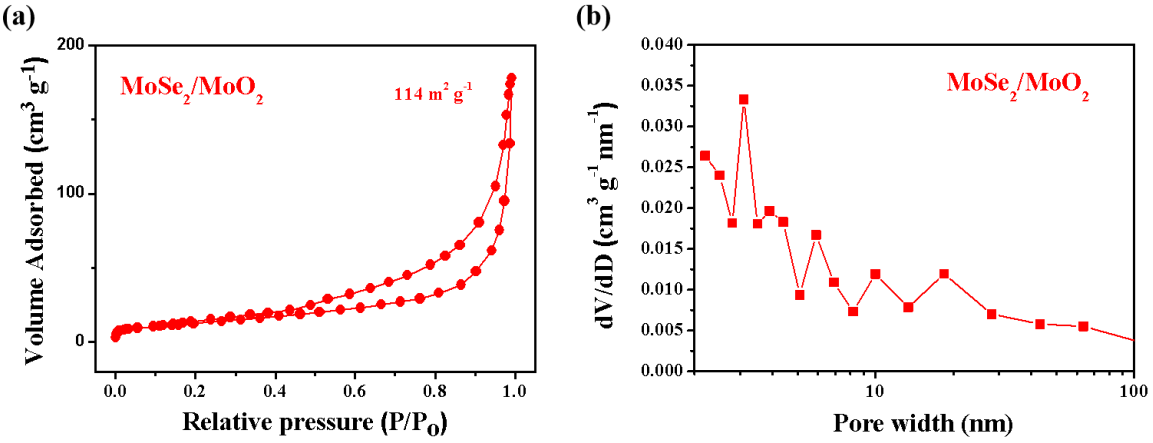

Figure 3. (**a**) N_2 adsorption/desorption isotherms of the $MoSe_2/MoO_2$ composite; (**b**) Pore-size distribution of the $MoSe_2/MoO_2$ composite.

The composition of the $MoSe_2/MoO_2$ composite is further characterized using X-ray photoelectron spectroscopy (XPS). Figure 4a shows the XPS survey spectrum of the $MoSe_2/MoO_2$ composite. The Mo 3d spectrum (Figure 4b) shows that the peaks at 231.7 eV for Mo $3d_{3/2}$ and 227.9 eV for Mo $3d_{5/2}$ are assigned to the Mo-Se bond in the $MoSe_2$ [31]. The other two peaks at 232.2 and 228.1 eV are attributed to the Mo $3d_{3/2}$ and Mo $3d_{5/2}$ of Mo^{4+} in the MoO_2, respectively [32]. Additionally, the peak at 235.2 eV corresponding to Mo $3d_{3/2}$ of Mo^{6+} can be ascribed to the slight oxidation of MoO_2 by calcination in the air atmosphere [33,34]. The Se XPS spectrum (Figure 4c) shows two peaks at 54.4 eV and 53.6 eV, corresponding to Se^{2-} in $MoSe_2$ [31]. The O 1s XPS peak (Figure 4d) corresponds to MoO_2 in the Mo(IV)-O bond at 531.1 eV, further confirming that the MoO_2 could be formed on the $MoSe_2$ in the calcination process [35]. Another peak located at 532.0 eV could be attributed to the trace water adsorbed.

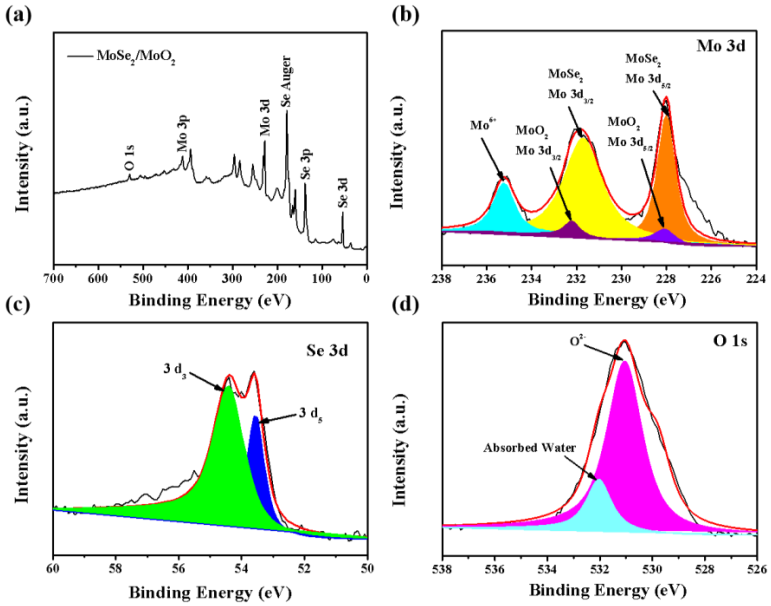

Figure 4. XPS spectra of the $MoSe_2/MoO_2$ composite: (**a**) a survey spectra; (**b**) Mo 3d; (**c**) Se 3d; (**d**) O 1s core level spectra.

Figure 5a shows CV curves for the initial three cycles of the $MoSe_2$ anode at 0.1 mV s^{-1}. The cathodic peaks observed at 1.26 V during the first cycle could be attributed to the insertion of Li^+ into $MoSe_2$ nanosheets to form Li_xMoSe_2 [36]. The cathodic peak at 0.45 V is assigned to the further conversion from Li_xMoSe_2 to Mo and Li_2Se, as well as the formation of solid electrolyte interphase (SEI) layer [37]. Hereafter, the cathodic peak appeared at 1.79 V is equivalent to the conversion of Se to Li_2Se and the association of Li with Mo. In the anodic process, the peak at 1.73 and 2.25 V correspond to the conversion of Li_2Se to Se and Mo to $MoSe_2$ [38]. It is noteworthy that the CV curves of the second and third cycles have large deviations in shape, indicating that the stability and reversibility of the $MoSe_2$ anode are poor.

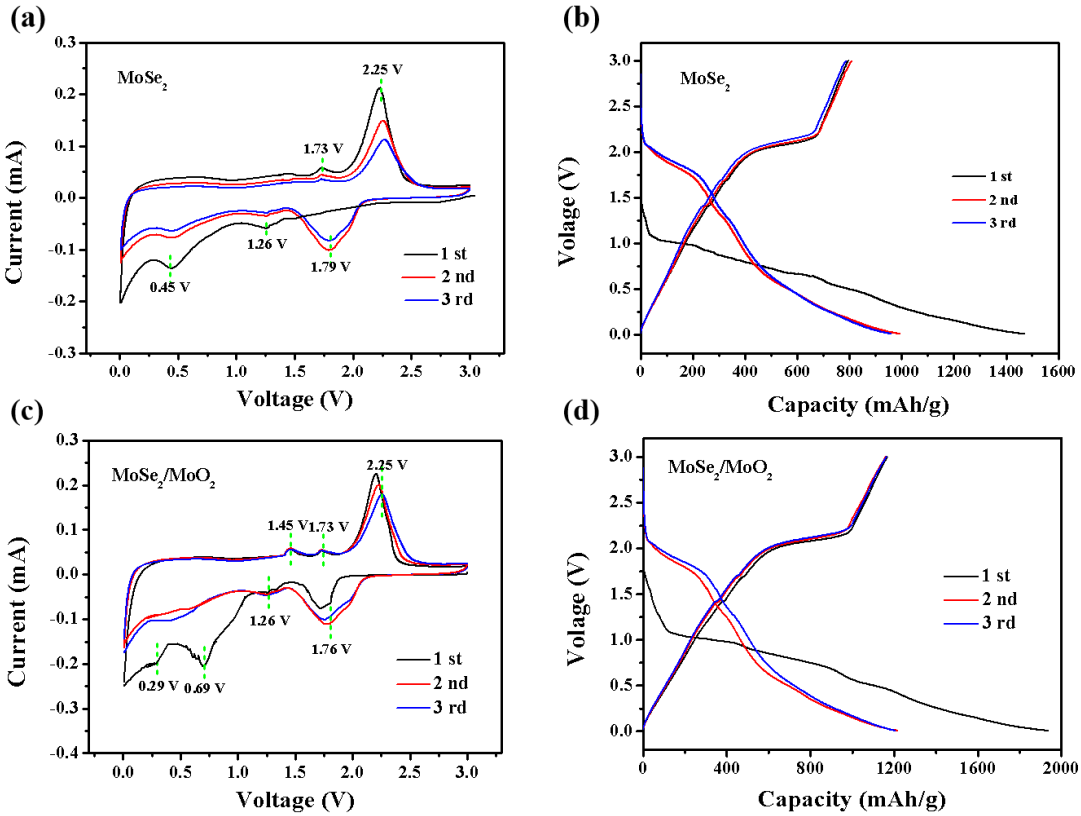

Figure 5. CV curves of (**a**) $MoSe_2$ and (**c**) $MoSe_2/MoO_2$ anodes in the potential range 0.01–3.0 V at a scan rate of 0.1 mV s^{-1}, The first three voltage-capacity profiles of (**b**) $MoSe_2$ and (**d**) $MoSe_2/MoO_2$ anode at a current density of 0.1 A g^{-1}.

Figure 5b shows the galvanostatic discharge-charge profiles of $MoSe_2$ anode at 0.1 A g^{-1}. The $MoSe_2$ anode delivers an initial discharge and charge capacity of 1473 mAh g^{-1} and 794 mAh g^{-1}, corresponding to an initial coulombic efficiency (CE) as low as 53.9%. In the second and third cycle, 80.9% and 83.0% efficiency can be observed, respectively. These values were much lower than those of the $MoSe_2/MoO_2$ anode.

The CV curves of the $MoSe_2/MoO_2$ anode are shown in Figure 5c. The cathodic peaks at 1.26 V and 1.76 V and the anodic peak at 2.25 V are similar to what observed in the CV curves of $MoSe_2$.In addition, the cathodic peak at 0.29 V represents the decomposition of $LixMoSe_2$ to Li_2Se and Mo in the first cycle and shifts to 0.45V in subsequent cycles. The formation of an SEI layer happens at around 0.69 eV [39]. The cathodic peaks at 1.50–2.00 V and the anodic peaks at 1.25–2.00 V could be attributed to the phase transition between the monoclinic and orthorhombic phases in the partially lithiated $LixMoO_2$ [40]. The peaks in the subsequent second to third cycles are almost overlapped at the same voltage, which indicates excellent chemical and structural stability of the $MoSe_2/MoO_2$ anode caused by the synergy in the $MoSe_2/MoO_2$ composite.

The first three galvanostatic discharge-charge profiles of $MoSe_2/MoO_2$ anode at 0.1 A g^{-1} are indicated in Figure 5d, where an initial discharge and charge capacity of 1926 mAh g^{-1} and 1174 mAh g^{-1} can be achieved. The corresponding low CE is about 60.9%, attributing to the formation of SEI film, which consumes some of the original lithium [41,42]. In the subsequent two cycles, the CE is about 96.3% and 97.1%. The capacity loss from the 1st to 2nd cycle could be ascribed to the irreversible reactions during the discharge/charge processes, such as the formation of SEI film. It indicates that $MoSe_2/MoO_2$ anode possess highly reversible specific capacities and cyclic stability. In addition, according to the results of XPS, the atomic contents of Mo, Se and O elements are 32.63%, 52.28%, and 15.09%, respectively. The results show that $MoSe_2$ and MoO_2 account for 78% and 22% of the composite. Therefore, it is calculated based on theoretical specific capacity of $MoSe_2$ (422 mAh g^{-1}) and MoO_2 (838 mAh g^{-1}) that the theoretical capacity of $MoSe_2/MoO_2$ anode is about 514 mAh g^{-1} lower than practical capacity of 1926 mAh g^{-1}, which is attributed to the synergistic effect of $MoSe_2$ and MoO_2.

The rate capability of the two anodes is compared in Figure 6a. $MoSe_2/MoO_2$ anode delivers the specific capacities of 1214, 1045, 903, 741, and 612 mAh g^{-1} at 0.1, 0.2, 0.5, 1, and 2 A g^{-1}, respectively. In contrast, the $MoSe_2$ anode only shows very low reversible capacities of 497 and 339 mAh g^{-1} at 1 and 2 A g^{-1}, respectively. When the current density is taken back to 0.1 A g^{-1}, it is noted that the capacity retention of the $MoSe_2/MoO_2$ anode reaches as high as 80.1%, indicating excellent rate capability of this anode. The cycling stability of $MoSe_2/MoO_2$ anode is evaluated at 0.1 A g^{-1}. As shown in Figure 6b, $MoSe_2/MoO_2$ anode exhibits a high specific capacity of 1042 mAh g^{-1} after 100 cycles, and the CE is close to 100%, indicating good cycling stability. For comparison, $MoSe_2$ anode only delivers a specific capacity of 581 mAh g^{-1} after 100 cycles.

The charge-discharge curves of $MoSe_2$ and $MoSe_2/MoO_2$ anode at different current densities after 1st cycle in the range of 0.01–3 V are shown in Figure 6c–d. At corresponding density, $MoSe_2/MoO_2$ anode shows a higher discharge specific capacity than $MoSe_2$ anode, and the charge and discharge platform is more obvious, even at 2 A g^{-1}, the shape of the charge and discharge platform is still very complete. The excellent long-term cycling behavior of $MoSe_2/MoO_2$ anode at 2 A g^{-1} is also exhibited in Figure 6e. The $MoSe_2/MoO_2$ anode preserves a high discharge capacity of 547 mAh g^{-1} with the CE close to 100% after 300 cycles. On the other hand, the $MoSe_2$ anode exhibits a discharge capacity of 202 mAh g^{-1}, much lower than $MoSe_2/MoO_2$ anode. The excellent electrochemical properties of $MoSe_2/MoO_2$ anode can be attributed to the promotion of Li^+ transport by $MoSe_2$ and protection of lamellar structure of $MoSe_2$ by MoO_2.

The EIS of both anodes is shown in Figure 7. All EIS plots consist of a semi-circle in the medium-high frequency region and a straight line in the low-frequency region, representing the charge transfer process and typical Warburg behavior. From the results, the optimized $MoSe_2/MoO_2$ anode shows a smaller semi-circle diameter than the $MoSe_2$ anode, indicating its lowest charge transfer resistance (77 Ω). In the low frequencies, as-prepared $MoSe_2/MoO_2$ composite has the largest slope demonstrating the best lithium diffusion efficiency, which means that the electrochemical reaction becomes easier than $MoSe_2$ anode [43]. It is contributed to the nanoscale combination effect promotes the diffusion and transfer of lithium, which is a key factor in obtaining high-performance LIBs.

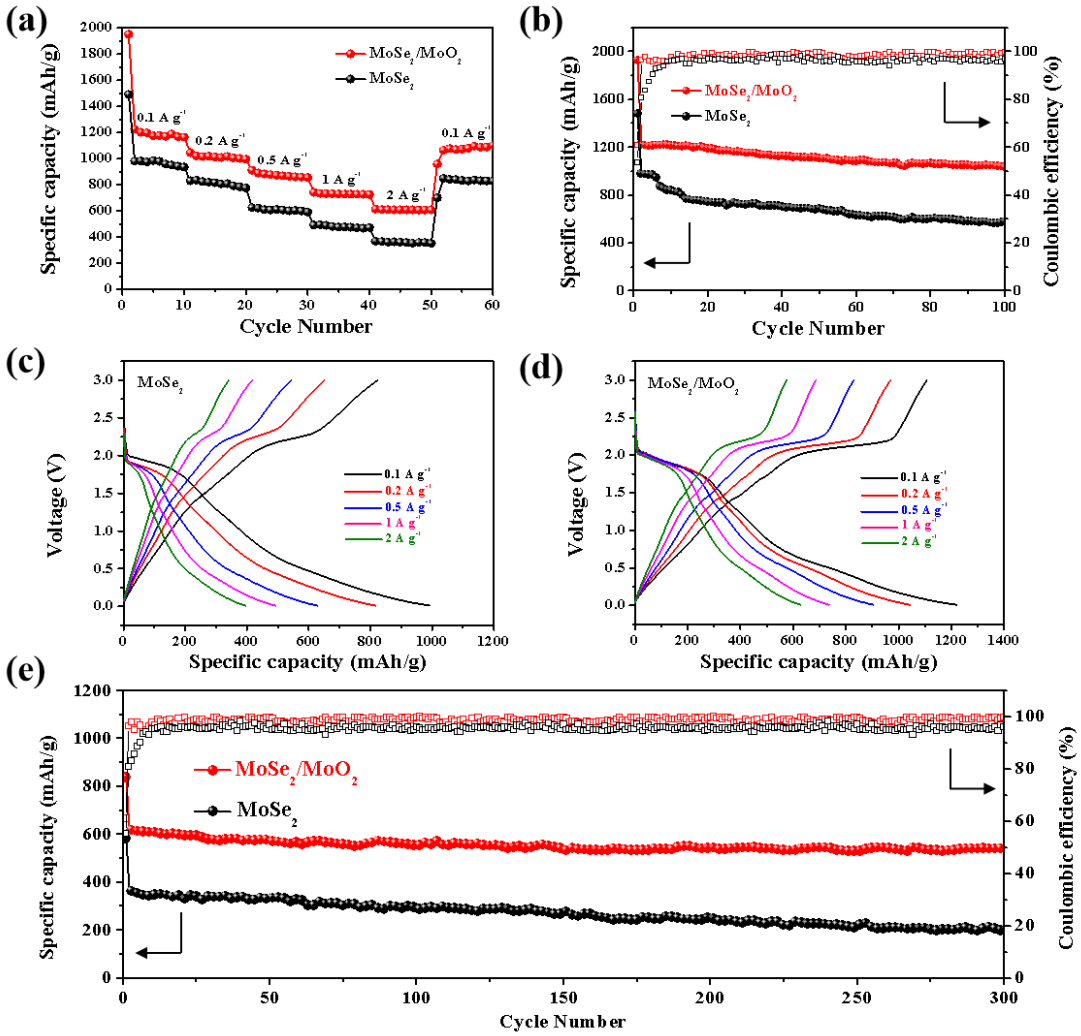

Figure 6. (**a**) Rate capacity at different current densities (increased from 0.1 A g^{-1} to 2 A g^{-1}) of the $MoSe_2$ and $MoSe_2/MoO_2$ anode; (**b**) Cycling performance of $MoSe_2$ and $MoSe_2/MoO_2$ anode at 0.1 A g^{-1}; (**c**–**d**) Charge-discharge curves of $MoSe_2$ and $MoSe_2/MoO_2$ anode at different current densities; (**e**) Long-term cycling performance of the $MoSe_2$ and $MoSe_2/MoO_2$ anode at a rate of 2 A g^{-1}.

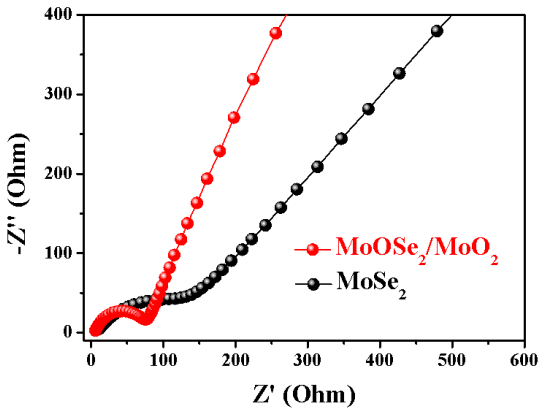

Figure 7. Nyquist plots for $MoSe_2$ and $MoSe_2/MoO_2$ anode.

4. Conclusions

$MoSe_2/MoO_2$ composite is obtained by a simple method with calcinating. It can alleviate huge volume variation of composite, promote the transmission of Li^+ and provide a high interfacial area

of electrode/electrolyte, which demonstrates excellent electrochemical properties. For example, the $MoSe_2/MoO_2$ composite exhibits a high capacity of 547 mAh g^{-1} after 300 cycles at 2 A g^{-1}. The simple and effective synthesis of this composite has great potential for the application of Selenium-based materials in LIBs.

Author Contributions: Formal Analysis—Y.Z. and Q.H.; Investigation—Q.H. and G.C.; Writing-Original Draft —Q.H. and G.C.; Writing-Review & Editing—Z.B. and Y.Z.; Supervision—Y.Z.; Project Administration—Y.Z.

Funding: This research was funded bythe Ministry of Education and Science of the Republic of Kazakhstan via the Targeted Program BR05236524 "Innovative materials and systems for energy conversion and storage" and a Small Grant from Nazarbayev University "Development of safe and high performance flexible Li-ion batteries".

Acknowledgments: This research was supported by the targeted state program No. BR05236524 "Innovative Materials and Systems for Energy Conversion and Storage" from the Ministry of Education and Science of the Republic of Kazakhstan and the Nazarbayev University by the research grant No.110119FD4504.

Conflicts of Interest: The authors declare no conflict of interest.

References

1. Chen, G.; Yan, L.; Luo, H.; Guo, S. Nanoscale engineering of heterostructured anode materials for boosting lithium-ion storage. *Adv. Mater.* **2016**, *28*, 7580–7602. [CrossRef]
2. Yan, J.; Zhu, B.; Lu, Z.; Liu, N.; Jia, Z. Challenges and recent progress in the development of Si anodes for lithium-ion battery. *Adv. Energy Mater.* **2017**, *7*, 1700715.
3. Choi, J.W.; Aurbach, D. Promise and reality of post-lithium-ion batteries with high energy densities. *Nat. Rev. Mater.* **2016**, *1*, 16013. [CrossRef]
4. Yu, S.H.; Feng, X.; Zhang, N.; Seok, J.; Abruña, H.D. Understanding conversion-type electrodes for lithium rechargeable batteries. *Acc. Chem. Res.* **2018**, *51*, 273–281. [CrossRef]
5. Yi, Z.; Wang, L.P.; Sougrati, M.T.; Feng, Z.; Leconte, Y.; Fisher, A.; Srinivasan, M.; Xu, Z. A review on design strategies for carbon based metal oxides and sulfides nanocomposites for high performance Li and Na ion battery anodes. *Adv. Energy Mater.* **2017**, *7*, 1601424.
6. Wang, S.; Guan, B.Y.; Yu, L.; Lou, X.W. Rational design of three-layered TiO_2@Carbon@MoS_2 hierarchical nanotubes for enhanced lithium storage. *Adv. Mater.* **2017**, *29*, 1702724. [CrossRef]
7. Zhou, X.; Le, Y.; Xiong, W.D.L. Formation of uniform N-doped carbon-coated SnO_2 submicroboxes with enhanced lithium storage properties. *Adv. Energy Mater.* **2016**, *6*, 1600451. [CrossRef]
8. Gang, H.; Feifei, Z.; Xinchuan, D.; Yuling, Q.; Dongming, Y.; Limin, W. Metal organic frameworks route to in situ insertion of multiwalled carbon nanotubes in Co_3O_4 polyhedra as anode materials for lithium-ion batteries. *ACS Nano* **2015**, *9*, 1592–1599.
9. Xue, H.; Jie, W.; Wang, S.S.; Muhammad, S.; Yun, Z. Core-shell MoS_2@graphene composite microspheres as stable anode for Li-ion batteries. *New J. Chem.* **2018**, *42*, 15340–15345. [CrossRef]
10. Le, S.; Zhao, T. Recent advances in inorganic 2D materials and their applications in lithium and sodium batteries. *J. Mater. Chem. A* **2017**, *5*, 3735–3758.
11. Ge, P.; Hou, H.; Banks, C.E.; Foster, C.W.; Li, S.; Zhang, Y.; He, J.; Zhang, C.; Ji, X. Binding $MoSe_2$ with carbon constrained in carbonous nanosphere towards high-capacity and ultrafast Li/Na-ion storage. *Energy Storage Mater.* **2018**, *12*, 310–323. [CrossRef]
12. Zhang, P.; Qin, F.; Zou, L.; Wang, M.; Zhang, K.; Lai, Y.; Li, J. Few-layered MoS_2/C with expanding d-spacing as a high-performance anode for sodium-ion batteries. *Nanoscale* **2017**, *9*, 12189–12195. [CrossRef]
13. Zhu, M.; Luo, Z.; Pan, A.; Yang, H.; Zhu, T.; Liang, S.; Cao, G. N-doped one-dimensional carbonaceous backbones supported $MoSe_2$ nanosheets as superior electrodes for energy storage and conversion. *Chem. Eng. J.* **2018**, *334*, 2190–2200. [CrossRef]
14. Tang, W.; Xie, D.; Shen, T.; Wang, X.; Wang, D.; Zhang, X.; Xia, X.; Wu, J.; Tu, J. Smart construction of nitrogen-doped carbon coated $MoSe_2$ microspheres with enhanced performance for lithium storage. *Chem. Eur. J* **2017**, *23*, 12924–12929. [CrossRef]
15. Zhao, X.; Sui, J.; Li, F.; Fang, H.; Wang, H.; Li, J.; Cai, W.; Cao, G. Lamellar $MoSe_2$ nanosheets embedded with MoO_2 nanoparticles: novel hybrid nanostructures promoted excellent performances for lithium ion batteries. *Nanoscale* **2016**, *8*, 17902. [CrossRef]

16. Jin, R.; Cui, Y.; Wang, Q.; Li, G. Facile fabrication of CNTs@C@$MoSe_2$@Se hybrids with amorphous structure for high performance anode in lithium-ion batteries. *J. Colloid Interface Sci.* **2017**, *508*, 435–442. [CrossRef]
17. Kang, J.; Su, Q.; Feng, H.; Huang, P.; Du, G.; Xu, B. $MoSe_2$ nanosheets-wrapped flexible carbon cloth as binder-free anodes for high-rate lithium and sodium ion storages. *Electrochim. Acta* **2019**, *301*, 29–38. [CrossRef]
18. Qin, F.; Hu, H.; Jiang, Y.; Kai, Z.; Zhao, F.; Lai, Y.; Jie, L. Mesoporous $MoSe_2$/C composite as anode material for sodium/lithium ion batteries. *J. Electroanal. Chem.* **2018**, *823*, 67–72. [CrossRef]
19. Eftekhari, A. Molybdenum diselenide ($MoSe_2$) for energy storage, catalysis, and optoelectronics. *Appl. Mater. Today* **2017**, *8*, 1–17. [CrossRef]
20. Xiang, T.; Tao, S.; Xu, W.; Fang, Q.; Wu, C.; Liu, D.; Zhou, Y.; Khalil, A.; Muhammad, Z.; Chu, W. Stable 1T-$MoSe_2$ and carbon nanotubes hybridized flexible film: Binder-free and high-performance Li-ion anode. *ACS Nano* **2017**, *11*, 6483–6491. [CrossRef]
21. Xie, D.; Xia, X.H.; Tang, W.J.; Zhong, Y.; Wang, Y.D.; Wang, D.H.; Wang, X.L.; Tu, J.P. Novel carbon channels from loofah sponge for construction of metal sulfide/carbon composites with robust electrochemical energy storage. *J. Mater. Chem. A* **2017**, *5*, 7578–7585. [CrossRef]
22. Ren, W.; Zhang, H.; Guan, C.; Cheng, C. Ultrathin MoS_2 nanosheets@ metal organic framework-derived n-doped carbon nanowall arrays as sodium ion battery anode with superior cycling life and rate capability. *Adv. Funct. Mater.* **2017**, *27*, 1702116. [CrossRef]
23. Cong, L.; Xie, H.; Li, J. Hierarchical structures based on two-dimensional nanomaterials for rechargeable lithium batteries. *Adv. Energy Mater.* **2017**, *7*, 1601906. [CrossRef]
24. Deng, M.; Qi, J.; Xiang, L.; Xiao, Y.; Yang, L.; Xiang, Y.; Hui, W.; Yuan, B.; Gao, Q. MoC/C nanowires as high-rate and long cyclic life anode for lithium ion batteries. *Electrochim. Acta* **2018**, *277*, 205–210. [CrossRef]
25. Sun, H.; Zhang, Y.; Liu, H.; Zhang, X.; Wang, J.G. Constructing hierarchical MoO_2/N-doped carbon hydrangea-like spheres with superior lithium storage properties. *J. Alloys Compd.* **2019**, *787*, 45–52. [CrossRef]
26. Li, X.; Xiao, Q.; Gao, Y.; Zhang, H.; Xu, H.; Zhang, Y. Hierarchical MoO_2/C microspheres: Preparation and application as anode materials for lithium ion batteries. *J. Alloys Compd.* **2017**, *723*, 1113–1120. [CrossRef]
27. Xu, G.; Ping, L.; Ren, Y.; Huang, X.; Wang, H. Three-dimensional MoO_2 nanotextiles assembled from elongated nanowires as advanced anode for Li ion batteries. *J. Power Sources* **2017**, *361*, 1–8. [CrossRef]
28. Qi, Y.; Zhou, B.; Zheng, S.; Yang, X.; Jin, W. 3D interconnected MoO_2 nanocrystals on nickel foam as binder-free anode for Li-ion batteries. *Mater. Sci. Ed.* **2018**, *33*, 1315–1322. [CrossRef]
29. Fu, H.; Xu, Z.; Wang, T.; Li, K.; Shen, X.; Li, J.; Huang, J. Rate behavior of MoO_2/graphene oxide lithium-ion battery anodes from electrochemical contributions. *J. Electrochem. Soc.* **2018**, *165*, A439–CA447. [CrossRef]
30. Wang, S.; Liu, B.; Zhi, G.; Xu, G.; Wang, Q.; Zhang, J. 2D layered mesoporous MoO_2/rGO composites for high performance anode materials in lithium-ion battery. *Microporous Mesoporous Mater.* **2017**, *246*, 14–23. [CrossRef]
31. Wu, S.; Yao, D.; Sun, S. Transition metal dichalcogenide based nanomaterials for rechargeable batteries. *Chem. Eng. J.* **2017**, *307*, 189–207. [CrossRef]
32. Yu, Z.; Hui, X.; Wang, C.; He, Q.; Qin, L.; Muhammad, Z.; Haleem, Y.A.; Yuan, S.; Chen, S.; Li, S. Probing lithium storage mechanism of MoO_2 nanoflowers with rich oxygen-vacancy grown on graphene sheets. *J. Phys. Chem. C* **2017**, *121*, 15589–15596.
33. Yun, Y.; Shi, Z.; Shao, J.; Qu, Q.; Gao, Y.; Chen, Z.; Chen, Y.; Zheng, H. Strongly surface-bonded MoO_2@Carbon nanocomposites by nitrogen-doping with outstanding capability for fast and stable Li storage. *Chem. Nanostruct. Mater.* **2018**, *4*, 1247–1253. [CrossRef]
34. Li, Q.; Qi, Y.; Zhao, Y.; Wan, B. Carbon-based coating containing ultrafine MoO_2 nanoparticles as an integrated anode for high-performance lithium-ion batteries. *J. Nano Res.* **2017**, *19*, 332. [CrossRef]
35. Zhou, E.; Wang, C.; Shao, M.; Deng, X.; Xu, X. MoO_2 nanoparticles grown on carbon fibers as anode materials for lithium-ion batteries. *Ceram. Int.* **2017**, *43*, 760–765. [CrossRef]
36. Hui, W.; Wang, X.; Li, W.; Jin, W.; Jiang, D.; Li, G.; Yan, Z.; Zhong, H.; Yang, J. Phase transition mechanism and electrochemical properties of nanocrystalline $MoSe_2$ as anode materials for the high performance lithium-ion battery. *J. Phys. Chem. C* **2015**, *119*, 10197–10205.
37. Xing, Y.; Zhang, Z.; Shi, X. Rational design of coaxial-cable $MoSe_2$/C: Towards high performance electrode materials for lithium-ion and sodium-ion batteries. *J. Alloys Compd.* **2016**, *686*, 413–420.

38. Yao, J.; Liu, B.; Ozden, S.; Wu, J.; Yang, S.; Rodrigues, M.T.F.; Kalaga, K.; Pei, D.; Peng, X.; Zhang, Y. 3D nanostructured molybdenum diselenide/graphene foam as anodes for long-cycle life lithium-ion batteries. *Electrochim. Acta* **2015**, *176*, 103–111. [CrossRef]
39. Liu, Y.; Zhu, M.; Chen, D. Sheet-like $MoSe_2$/C composites with enhanced Li-ion storage properties. *J. Mater. Chem. A* **2015**, *3*, 11857–11862. [CrossRef]
40. Ying, W.; Huang, Z.; Wang, Y. A new approach to synthesize MoO_2@C for high-rate lithium ion batteries. *J. Mater. Chem. A* **2015**, *3*, 21314–21320.
41. Huang, B.; Li, X.; Pei, Y.; Li, S.; Cao, X.; Massé, R.C.; Cao, G. Novel carbon-encapsulated porous SnO_2 anode for lithium-ion batteries with much improved cyclic stability. *Small* **2016**, *12*, 1945–1955. [CrossRef]
42. Devina, W.; Hwang, J.; Kim, J. Synthesis of MoO_2/Mo_2C/RGO composite in supercritical fluid and its enhanced cycling stability in Li-ion batteries. *Chem. Eng. J.* **2018**, *345*, 1–12. [CrossRef]
43. Zhang, Y.; Rui, X.; Tang, Y.; Liu, Y.; Chen, X. Wet-chemical processing of phosphorus composite nanosheets for high-rate and high-capacity lithium-ion batteries. *Adv. Energy Mater.* **2016**, *6*, 1502409. [CrossRef]